

Zero-shot 3D Segmentation of Abdominal Organs in CT Scans Using Segment Anything Model 2: Adapting Video Tracking Capabilities for 3D Medical Imaging

Yosuke Yamagishi, MD^{1*}, Shouhei Hanaoka, MD, PhD^{1,2}, Tomohiro Kikuchi, MD, MPH, PhD^{3,4}, Takahiro Nakao, MD, PhD⁴, Yuta Nakamura, MD, PhD⁴, Yukihiro Nomura, PhD^{4,5}, Soichiro Miki, MD, PhD⁴, Takeharu Yoshikawa, MD, PhD⁴, Osamu Abe, MD, PhD^{1,2}

1. Division of Radiology and Biomedical Engineering, Graduate School of Medicine, The University of Tokyo
2. Department of Radiology, The University of Tokyo Hospital
3. Department of Radiology, School of Medicine, Jichi Medical University
4. Department of Computational Diagnostic Radiology and Preventive Medicine, The University of Tokyo Hospital
5. Center for Frontier Medical Engineering, Chiba University

* yamagishi-yosuke0115@g.ecc.u-tokyo.ac.jp

Abstract

Purpose:

To evaluate the zero-shot performance of Segment Anything Model 2 (SAM 2) in 3D segmentation of abdominal organs in CT scans, and to investigate the effects of prompt settings on segmentation results.

Materials and Methods:

Using a subset of the TotalSegmentator CT dataset (n = 123) from eight institutions, we assessed SAM 2's ability to segment eight abdominal organs. Segmentation was initiated from three different z-coordinate levels (caudal, mid, and cranial levels) of each organ. Performance was measured using the Dice similarity coefficient (DSC). We also analyzed the impact of "negative prompts," which explicitly exclude certain regions from the segmentation process, on accuracy. Additionally, we analyzed organ volumes to contextualize the segmentation performance.

Results:

As a zero-shot approach, larger organs with clear boundaries demonstrated high segmentation performance, with mean(median) DSCs as follows: liver 0.821(0.898), left kidney 0.870(0.921), right kidney 0.862(0.935), and spleen 0.891(0.932). Smaller organs showed lower performance: gallbladder 0.531(0.590), pancreas 0.361(0.359), and adrenal glands, right 0.203(0.109), left 0.308(0.231). The initial slice for segmentation and the use of negative prompts significantly influenced the results. By removing negative prompts from the input, the DSCs significantly decreased for six organs. Moderate positive correlations were observed between volume sizes and DSCs.

Conclusion:

SAM 2 demonstrated promising zero-shot performance in segmenting certain abdominal organs in CT scans, particularly larger organs with clear boundaries. Performance was significantly influenced by input negative prompts and initial slice selection, highlighting the importance of optimizing these factors for effective segmentation.

Introduction

Medical image segmentation is a critical task in radiology, playing a vital role in diagnosis, treatment planning, and clinical research (1,2). Traditionally, this process has been labor-intensive, requiring manual delineation by skilled radiologists. However, recent advancements in deep learning have revolutionized this field, dramatically expanding the scope of automated analysis and significantly enhancing performance across diverse medical imaging tasks.

The Segment Anything Model (SAM), introduced by Meta AI, represented a significant leap forward in image segmentation technology (3). Trained on over a billion masks, SAM demonstrated remarkable versatility in segmenting a wide array of objects across various domains. SAM's zero-shot performance - its ability to segment objects it has never seen during training - in medical images has been extensively evaluated (4,5), and specialized models such as MedSAM (6), which underwent additional training for medical imaging applications, have been introduced. These developments have demonstrated SAM's potential as a promising model in radiological domains, including CT and MRI. However, SAM was primarily designed for 2D image segmentation, which imposed inherent limitations on its direct applicability to 3D volumetric data.

The release of SAM 2 in July 2024 has extended these capabilities to video segmentation (7), opening new possibilities for application in medical imaging, particularly in the analysis of 3D volumetric data such as CT scans. While SAM 2 was not specifically designed for medical applications, its zero-shot ability presents an intriguing opportunity for adaptation to medical imaging tasks. The model's video tracking capabilities suggest a novel approach to 3D medical image segmentation, treating volumetric scans as sequences of 2D slices analogous to video frames. This approach could potentially overcome limitations of traditional 3D segmentation methods, which often require extensive training on domain-specific datasets.

While SAM 2's performance has been evaluated in surgical video segmentation (e.g., EndoVIS (8)) and specialized versions like Medical SAM2 have been developed (9), an assessment combining both its zero-shot performance and the effects of various input factors in radiology remains limited. Our research focuses on evaluating SAM 2's zero-shot performance in medical imaging and key input factors that influence its performance in this context. We examine how the model's performance varies with target organ size, from large structures like the liver to smaller ones like the adrenal glands. Additionally, we investigate two critical input factors that correspond to setting prompts: the choice of the initial slice within the 3D volume and the use of negative prompts to indicate non-target structures. SAM 2 allows for the selection of the starting slice position in medical imaging at the beginning of inference, which can significantly impact segmentation results. Furthermore, SAM 2's capability to incorporate negative prompts to indicate regions outside the area of interest presents a potential for enhancing segmentation accuracy.

To our knowledge, this comprehensive evaluation combining zero-shot performance assessment and input factor analysis is the first of its kind for SAM 2 applied to 3D medical imaging. In this sense, our exploration can be likened to prompt engineering in large language models, where the performance of the model is highly dependent on the design and optimization of input prompts. By examining the utility of prompt engineering in the context of segmentation, we aim to provide deeper insights into the adaptation of general-purpose AI models for specialized medical imaging applications.

Materials and Methods

This study was conducted as a retrospective study. Since the study used an open dataset, approval from the institutional review board was not necessary. This study adheres to the Checklist for Artificial Intelligence in Medical Imaging (CLAIM): 2024 Update (10).

Dataset

We aimed to evaluate the segmentation performance of major organs within the imaging range of abdominal CT, one of the most common medical imaging modalities. To conduct this performance evaluation, we utilized a subset of the TotalSegmentator CT dataset version 1.0 (11). The TotalSegmentator dataset is a large-scale, multi-organ segmentation dataset collected from multiple institutions. We selected this dataset for its comprehensive organ segmentation masks and institutional metadata for each case.

Our study included cases that encompassed the abdominal region, while CT angiography scans were excluded from the analysis.

To ensure representation from all 8 institutions while managing the dataset size, we implemented a sampling strategy. We set a maximum of 20 cases per institution and randomly selected cases up to this limit. For institutions with fewer than 20 cases, all available cases were included.

We focused on 8 major abdominal organs for our analysis:

1. Liver
2. Right Kidney
3. Left Kidney
4. Spleen
5. Gallbladder
6. Pancreas
7. Right Adrenal Gland
8. Left Adrenal Gland

These organs were chosen based on their clinical significance and visibility in standard abdominal CT scans. To account for potential annotation deficiencies, we excluded extremely small volume masks by setting a threshold of 100 voxels. Masks below this threshold were omitted from the analysis.

Data Preprocessing

The dataset was available in NIfTI file format. For SAM 2 inference, we extracted each horizontal slice from the 3D volumes to create subsets of 2D images for each scan. We applied windowing to the CT scans, using a window level of 50 and a window width of 400 Hounsfield units. Following windowing, we performed min-max scaling on the data. The scaled values were then converted to 8-bit integers, resulting in a range of 0-255. These processed 2D images were saved as sequential JPEG files.

For SAM 2 inference, we selectively processed only the slices containing abdominal organs. This approach focused on optimizing computational efficiency, resulting in faster inference speeds.

Analysis of Organ Mask Volumes

For the volumetric analysis, we utilized the existing segmentation masks from the TotalSegmentator dataset to calculate the volume of each organ in voxels. We chose to measure in voxels rather than physical units because our model inputs do not consider voxel scale.

Additionally, we analyzed cross-sectional areas of organ masks along the z-axis. For each organ, we calculated mean mask areas at the 25th, 50th, and 75th percentile z-coordinates, corresponding to the initial prompt locations used in SAM 2 segmentation.

SAM 2 Implementation for 3D Medical Image Segmentation

SAM 2 is a segmentation model not specifically designed for medical images, but rather for general videos, such as sports or animal videos. These models are trained on a large dataset, enabling them to perform segmentation on any objects. SAM 2's main feature is its ability to support not only 2D

images but also videos. By inputting coordinates indicating the target object for segmentation, SAM 2 can track and segment objects appearing within the video. An overview of CT volume segmentation using SAM 2's video predictor is shown in Figure 1.

- *Adaptation for 3D Medical Imaging*

Although SAM 2 was originally intended for tracking objects in general videos, we recognized that 3D volumes like CT and MRI scans can be considered as videos composed of numerous 2D images. Utilizing publicly available datasets with segmentation masks, we applied preprocessing compatible with SAM 2's video prediction capabilities. This allowed us to construct a pipeline capable of performing multi-organ segmentation in a zero-shot manner, without additional training of SAM 2.

- *Bidirectional Prediction Approach*

While SAM 2's video prediction is unidirectional, it can process in both directions from the initial frame. To obtain a complete segmentation mask for the entire volume, we implemented a simple bidirectional approach: we performed inference in both the forward direction from the starting slice to the most cranial slice, and in the reverse direction from the starting slice to the most caudal slice. The two segmentation masks obtained from these bidirectional inferences were then merged to create a full 3D segmentation mask.

- *Model Inference and Prompt Setting*

SAM 2's video prediction requires input of both the video (numbered 2D images) and prompt (coordinates for the target object). In practice, the prompt must be manually specified by a user. However, given the need to evaluate a large number of objects, we devised an algorithm to automatically obtain prompts:

1. Z-coordinate focus: Using 25th (caudal-level), 50th (mid-level), and 75th percentiles (cranial-level) for comprehensive organ representation.
2. Random selection within organ boundaries:
 - Five positive prompts from within the segmentation mask
 - Five negative prompts were sampled from the region 2-3 voxels outside the mask boundary, excluding the immediate 1-voxel margin

This method maintains reproducibility, reduces bias from the user's prompting skill, and leverages SAM 2's capability to use both positive and negative prompts for improved accuracy.

In this study, we refer to the 3D segmentations initiated from each of these positions as caudal-approach, mid-approach, and cranial-approach, corresponding to segmentations starting from the caudal, mid, and cranial-level slices, respectively.

- *Model Version*

For our study, we selected the "sam2_hiera_large" model, due to its highest performance among the available versions. We used version 1.0 of the SAM 2 (<https://github.com/facebookresearch/segment-anything-2>). Our implementation was carried out using Python 3.10.12.

Statistical Analysis:

To evaluate the model's performance, we calculated the Dice similarity coefficient (DSC). This evaluation was performed organ-wise across the dataset to provide a detailed analysis.

We compared the segmentation performance across the different approaches and with/without negative prompts. We performed three pairwise comparisons for the approaches: caudal-approach vs mid-approach, caudal-approach vs cranial-approach, and mid-approach vs cranial-approach. Additionally, we compared performance with and without negative prompts.

To account for multiple comparisons, we applied the Bonferroni correction. After Bonferroni correction, a P value $<0.05/3$ (approximately 0.0167) was considered statistically significant.

All statistical analyses were conducted using SciPy version 1.14.0.

Results

Dataset

Our sampling strategy resulted in a total of 123 scans. Twenty scans each were selected from five institutions, while the remaining three institutions contributed 5, 5, and 13 cases respectively. The dataset selection process is detailed in Figure 2. The average age of the patients in our selected sample was 60.7 years (standard deviation [SD] 15.5). The gender distribution consisted of 63 males and 60 females.

903 organ segmentations were obtained from 123 scans. 12 masks with volumes of 100 voxels or smaller were then excluded from the analysis. The final dataset consisted of 891 organ segmentations.

Analysis of Organ Mask Volumes and Areas

Organ volumes were detailed in Table 1, measured in voxels. The liver was the largest organ, followed by the spleen. Kidneys were the next largest, with similar volumes for left and right. Compared to the liver's mean volume, the pancreas was approximately 1/25, the gallbladder less than 1/70, and both adrenal glands less than 1/400 in size. These latter organs (pancreas, gallbladder, and adrenal glands) can be categorized as small organs.

Organ cross-sectional area analysis showed diverse trends across 8 organs. The liver was largest, increasing caudally to cranially. The pancreas steadily increased. Adrenal glands, though smallest, peaked at mid-level. Details in Supplemental Figure 1.

Multi-organ Segmentation Performance

We evaluated the performance for multi-organ segmentation using different starting slice positions. DSC are reported as mean(median) to reflect performance variability. All results are detailed in Table 2.

The left kidney demonstrated the best overall performance, maintaining high DSCs across all starting positions: 0.870(0.921), 0.825(0.918), and 0.808(0.912) for the caudal-approach, mid-approach, and cranial-approach, respectively. Notably, it was the only organ showing no statistically significant differences between any starting positions (all $P > .0167$).

The box plots (Figure 3) show that for all organs, the highest DSCs reached above 0.8, with some approaching or nearly reaching 1.0. However, the box plots also reveal instances of very low DSC values approaching 0 across various organs and approaches, indicating significant variability in segmentation performance.

Starting slice level had a significant impact on most organs. Organs demonstrated various patterns in segmentation performance depending on the starting level. The liver showed a significant decrease in performance as the starting position moved superiorly, with DSC dropping from 0.821(0.898) with caudal-approach to 0.702(0.786) with cranial-approach ($P < .01$). Smaller organs, such as the pancreas, adrenal glands, and gallbladder, showed the most pronounced impact of starting position. For these organs, performance significantly decreased when changing from a caudal-approach to a cranial-approach (all $P < .01$).

Larger organs, such as liver, kidneys, and spleen, consistently demonstrated higher DSCs compared to smaller organs across all approaches. When considering organ volumes in detail, we calculated Spearman's correlation coefficients to examine the relationship between object volumes and DSCs.

A moderate correlation was observed across all settings when using caudal-approach ($r_s = 0.731$, $P < .01$), mid-approach ($r_s = 0.698$, $P < .01$), and cranial-approach ($r_s = 0.699$, $P < .01$) (12,13). As shown in Table 3, when correlation coefficients were calculated separately for each organ, fair correlations were demonstrated for almost all items, particularly in smaller organs.

We also investigated the impact of including negative prompts on segmentation performance across different organs, focusing specifically on the caudal-approach (Table 4 and Supplemental Figure 2). All organs except the liver ($P = 0.32$) and spleen ($P = 0.27$) demonstrated significant increases in DSC ($P < .01$) with the inclusion of negative prompts.

Next, in Figure 4, we show the highest DSC masks, excluding cases where the ground truth segmentations were incomplete. The highest-performing masks, as visualized, generated for each organ in 3D were nearly indistinguishable from the ground truth.

On the other hand, there were cases where the performance fluctuated significantly due to differences in the approach. We present an example of the liver segmentation results in Figure 5. The DSC seemingly decreased by 0.564 (from 0.924 with caudal-approach to 0.360 with cranial-approach). For the caudal-approach, the initial slice segmentation appears to have been easier due to clear contrast with the surroundings. The cranial-approach, however, likely struggled with unclear boundaries between the liver, inferior vena cava, and abdominal wall, potentially leading to incomplete masking or incorrect inclusion of the inferior vena cava. This may have affected 3D mask generation for caudal slices, possibly resulting in low DSC. This example suggests the crucial role that accurate initial 2D mask segmentation might play in overall performance.

Discussion

To our knowledge, this is the first research that not only validates the performance of zero-shot SAM 2 on radiology images but also considers the impact of prompt input strategies, such as slice positioning and negative prompts. Our findings demonstrate the potential of SAM 2, a general-purpose segmentation model, in segmenting abdominal organs from CT scans. While prior studies have explored segmentation in CT and MRI (14), integrating their findings with our insights could drive further performance enhancements. A key advantage of SAM 2 is its ability to generate segmentation masks with just a few clicks on a single slice, drastically reducing the workload for radiologists who previously relied on labor-intensive manual annotations. Furthermore, optimizing prompt input strategies is essential for achieving even greater model performance.

SAM2 showed promising performance for larger organs with clear boundaries, such as the liver, kidneys, and spleen, achieving mean(median) DSC of 0.821(0.898)-0.891(0.932). Although SAM 2 was not specifically designed for medical image analysis, its notable performance suggests potential applicability to a wide range of any organ and lesion. While the scores are lower compared to previous supervised methods, which can achieve mean DSCs in the upper 0.9 range for some organs, they are still notably high for a zero-shot prediction. Moreover, the ability to segment an entire 3D volume by simply selecting and clicking on a target structure in a single slice is particularly significant.

The choice of initial prompt position had a significant impact on segmentation accuracy and the optimal position depended on the organ. This emphasizes that performance is highly dependent on the choice of initial slice. Excluding negative prompts led to a significant decrease in DSC for all organs except the spleen and liver, highlighting their importance in segmentation accuracy. Segmentation performance can be inferred to depend on multiple factors related to the 3D morphology, volume size, and contrast with surrounding tissues of target structure. These findings suggest the importance of optimizing prompts taking into account the characteristics of the targeted structure.

SAM 2 struggled with smaller and less defined structures such as the adrenal glands, pancreas, and gallbladder, resulting in lower DSCs. Interestingly, we observed a moderate positive correlation between organ volume and DSCs (Spearman's $r_s = 0.731$, $P < .01$), suggesting that volume size is one of several key factors influencing segmentation accuracy. This aligns with challenges typically observed in abdominal organ segmentation, even with supervised 3D models. Notably, supervised approaches like TotalSegmentator (based on nnUNet (15)), UNet (16), SegUNet (17), and SwinUNETR (18) also tend to show lower DSC for bilateral adrenal glands and gallbladder compared to other organs (19), a trend mirrored in SAM 2's performance.

Our study had several limitations. Firstly, our validation dataset was limited to abdominal CT scans, one of the most standard modalities. There are publicly available datasets such as Vertebral Segmentation, TotalSegmentator's MRI and Duke Liver datasets (20–22), which include segmentation masks for various anatomical structures and modalities. Expanding our validation using these resources would allow for a more robust evaluation. Additionally, as our approach was designed to address zero-shot performance validation, we did not perform any additional training such as fine-tuning. Performance improvements can be expected by using task-specific supervised methods instead of zero-shot. Furthermore, while we used an automated approach to evaluate a large number of organs, there is potential for improved accuracy through manual prompts inputting.

In conclusion, SAM 2 has demonstrated promising zero-shot performance in segmenting certain abdominal organs in CT scans, particularly larger organs with clear boundaries, highlighting its potential for cross-domain generalization in medical imaging. However, further improvements are needed for smaller and less distinct structures. Our study underscores the importance of applying general models to unseen medical images and optimizing input prompts, which together could significantly enhance the accuracy of medical image segmentation.

References

1. Wang S, Summers RM. Machine learning and radiology. *Medical Image Analysis*. 2012;16(5):933–951. doi: 10.1016/j.media.2012.02.005.
2. Saba L, Biswas M, Kuppili V, et al. The present and future of deep learning in radiology. *European Journal of Radiology*. 2019;114:14–24. doi: 10.1016/j.ejrad.2019.02.038.
3. Kirillov A, Mintun E, Ravi N, et al. Segment Anything. arXiv; 2023. doi: 10.48550/arXiv.2304.02643.
4. Mazurowski MA, Dong H, Gu H, Yang J, Konz N, Zhang Y. Segment anything model for medical image analysis: An experimental study. *Medical Image Analysis*. 2023;89:102918. doi: 10.1016/j.media.2023.102918.
5. Roy S, Wald T, Koehler G, et al. SAM.MD: Zero-shot medical image segmentation capabilities of the Segment Anything Model. arXiv; 2023. doi: 10.48550/arXiv.2304.05396.
6. Ma J, He Y, Li F, Han L, You C, Wang B. Segment anything in medical images. *Nat Commun*. Nature Publishing Group; 2024;15(1):654. doi: 10.1038/s41467-024-44824-z.
7. Ravi N, Gabeur V, Hu Y-T, et al. SAM 2: Segment Anything in Images and Videos. arXiv; 2024. <http://arxiv.org/abs/2408.00714>. Accessed August 2, 2024.
8. Allan M, Kondo S, Bodenstedt S, et al. 2018 Robotic Scene Segmentation Challenge. arXiv; 2020. doi: 10.48550/arXiv.2001.11190.
9. Zhu J, Qi Y, Wu J. Medical SAM 2: Segment medical images as video via Segment Anything Model 2. arXiv; 2024. <http://arxiv.org/abs/2408.00874>. Accessed August 7, 2024.
10. Tejani AS, Klontzas ME, Gatti AA, et al. Checklist for Artificial Intelligence in Medical Imaging (CLAIM): 2024 Update. *Radiology: Artificial Intelligence*. Radiological Society of North America; 2024;6(4):e240300. doi: 10.1148/ryai.240300.
11. Wasserthal J, Breit H-C, Meyer MT, et al. TotalSegmentator: Robust Segmentation of 104 Anatomic Structures in CT Images. *Radiol Artif Intell*. 2023;5(5):e230024. doi: 10.1148/ryai.230024.
12. Akoglu H. User's guide to correlation coefficients. *Turk J Emerg Med*. 2018;18(3):91–93. doi: 10.1016/j.tjem.2018.08.001.
13. Chan YH. Biostatistics 104: correlational analysis. *Singapore Med J*. 2003;44(12):614–619. Accessed August 10, 2024.
14. Ma J, Kim S, Li F, et al. Segment Anything in Medical Images and Videos: Benchmark and Deployment. arXiv; 2024. doi: [10.48550/arXiv.2408.03322](https://doi.org/10.48550/arXiv.2408.03322).
15. Isensee F, Jaeger PF, Kohl SAA, Petersen J, Maier-Hein KH. nnU-Net: a self-configuring method for deep learning-based biomedical image segmentation. *Nat Methods*. Nature Publishing Group; 2021;18(2):203–211. doi: 10.1038/s41592-020-01008-z.
16. Ronneberger O, Fischer P, Brox T. U-Net: Convolutional Networks for Biomedical Image Segmentation. In: Navab N, Hornegger J, Wells WM, Frangi AF, editors. *Medical Image Computing and Computer-Assisted Intervention – MICCAI 2015*. Cham: Springer International Publishing; 2015. p. 234–241. doi: 10.1007/978-3-319-24574-4_28.
17. Chen X, Cheng G, Cai Y, Wen D, Li H. Semantic Segmentation with Modified Deep Residual Networks. In: Tan T, Li X, Chen X, Zhou J, Yang J, Cheng H, editors. *Pattern Recognition*. Singapore: Springer; 2016. p. 42–54. doi: 10.1007/978-981-10-3005-5_4.
18. Swin UNETR: Swin Transformers for Semantic Segmentation of Brain Tumors in MRI Images | SpringerLink. . https://link.springer.com/chapter/10.1007/978-3-031-08999-2_22. Accessed August 8, 2024.
19. Li W, Yuille A, Zhou Z. How Well Do Supervised 3D Models Transfer to Medical Imaging Tasks? The Twelfth International Conference on Learning Representations. 2024. <https://openreview.net/forum?id=AhizIPytk4>. Accessed August 10, 2024.

20. Macdonald JA, Zhu Z, Konkel B, Mazurowski MA, Wiggins WF, Bashir MR. Duke Liver Dataset: A Publicly Available Liver MRI Dataset with Liver Segmentation Masks and Series Labels. *Radiol Artif Intell.* 2023;5(5):e220275. doi: 10.1148/ryai.220275.
21. Löffler MT, Sekuboyina A, Jacob A, et al. A Vertebral Segmentation Dataset with Fracture Grading. *Radiol Artif Intell.* 2020;2(4):e190138. doi: 10.1148/ryai.2020190138.
22. D'Antonoli TA, Berger LK, Indrakanti AK, et al. TotalSegmentator MRI: Sequence-Independent Segmentation of 59 Anatomical Structures in MR images. *arXiv*; 2024. doi: 10.48550/arXiv.2405.19492.

organ	mean	median	std	min	max	n
Liver	465,008.60	440,518	156,091.00	19,768	963,401	119
Right Kidney	39,381.57	42,008	18,122.20	216	79,713	108
Left Kidney	41,246.74	42,618	21,144.60	666	129,706	111
Spleen	71,730.34	59,338.5	45,884.40	13,818	303,676	115
Gallbladder	6,247.61	6,018	4,902.72	170	20,763	89
Pancreas	18,526.41	19,626	8,502.56	707	37,855	116
Right Adrenal Gland	1,101.86	1,111	465.47	216	2,590	118
Left Adrenal Gland	1,259.03	1,205	522.81	135	2,977	115

Table 1: Descriptive Statistics of Organ Volumes in Voxels Derived from CT Scan Mask Volumes. The table presents the statistics (mean, standard deviation, median, minimum, maximum, and number of organs) for each organ.

organ	approach	mean	median	std	min	max	<i>P</i> value
Liver	caudal	0.821	0.898	0.192	0.016	0.971	caudal vs mid: <.01 caudal vs cranial: <.01 mid vs cranial: 0.07
	mid	0.754	0.860	0.223	0.186	0.966	
	cranial	0.702	0.786	0.259	0.053	0.970	
Right Kidney	caudal	0.862	0.919	0.189	0.018	0.977	caudal vs mid: 0.03 caudal vs cranial: 0.16 mid vs cranial: <.01
	mid	0.862	0.935	0.212	0.017	0.974	
	cranial	0.801	0.918	0.270	0.000	0.964	
Left Kidney	caudal	0.870	0.921	0.154	0.000	0.968	caudal vs mid: 0.40 caudal vs cranial: 0.15 mid vs cranial: 0.15
	mid	0.825	0.918	0.221	0.003	0.973	
	cranial	0.808	0.912	0.242	0.000	0.966	
Spleen	caudal	0.891	0.932	0.131	0.008	0.981	caudal vs mid: <.01 caudal vs cranial: 0.0170 mid vs cranial: 0.56
	mid	0.839	0.918	0.187	0.130	0.980	
	cranial	0.768	0.928	0.302	0.025	0.982	
Gallbladder	caudal	0.527	0.547	0.288	0.001	0.939	caudal vs mid: 0.95 caudal vs cranial: <.01 mid vs cranial: 0.08
	mid	0.531	0.590	0.291	0.000	0.947	
	cranial	0.461	0.489	0.314	0.000	0.937	
Pancreas	caudal	0.353	0.371	0.168	0.004	0.851	caudal vs mid: 0.92 caudal vs cranial: <.01 mid vs cranial: <.01
	mid	0.361	0.359	0.197	0.000	0.773	
	cranial	0.287	0.261	0.209	0.000	0.763	
Right Adrenal Gland	caudal	0.203	0.109	0.222	0.000	0.849	caudal vs mid: <.01 caudal vs cranial: <.01 mid vs cranial: <.01
	mid	0.177	0.067	0.235	0.000	0.858	
	cranial	0.112	0.038	0.178	0.000	0.798	
Left Adrenal Gland	caudal	0.308	0.231	0.234	0.002	0.844	caudal vs mid: <.01 caudal vs cranial: <.01 mid vs cranial: 0.08
	mid	0.252	0.174	0.226	0.000	0.805	
	cranial	0.226	0.107	0.238	0.000	0.859	

Table 2: DSCs for multi-organ segmentation by different approaches (caudal, mid, and cranial). The table presents the statistics (mean, standard deviation, median, minimum, and maximum) for each organ by different approaches. *P* values from Wilcoxon signed-rank tests are provided for comparisons between approaches (caudal vs mid, caudal vs cranial, and mid vs cranial).

organ	r_s (caudal)	r_s (mid)	r_s (cranial)
Liver	0.328 ($P < .01$)	0.0489 ($P = 0.597$)	0.163 ($P = 0.0757$)
Right Kidney	0.231 ($P = 0.0164$)	0.347 ($P < .01$)	0.509 ($P < .01$)
Left Kidney	-0.0107 ($P = 0.912$)	0.293 ($P < .01$)	0.295 ($P < .01$)
Spleen	0.38 ($P < .01$)	0.307 ($P < .01$)	0.355 ($P < .01$)
Gallbladder	0.499 ($P < .01$)	0.509 ($P < .01$)	0.469 ($P < .01$)
Pancreas	0.475 ($P < .01$)	0.386 ($P < .01$)	0.379 ($P < .01$)
Right Adrenal Gland	0.371 ($P < .01$)	0.424 ($P < .01$)	0.278 ($P < .01$)
Left Adrenal Gland	0.452 ($P < .01$)	0.339 ($P < .01$)	0.447 ($P < .01$)

Table 3: Spearman correlation coefficients between ground truth of organ volumes and DSCs in caudal, mid, and cranial levels.

organ	mean	median	std	mean difference	median difference	<i>P</i> value
Liver	0.785	0.896	0.244	-0.036	-0.002	0.32
Right Kidney	0.858	0.910	0.203	-0.004	-0.009	<.01
Left Kidney	0.847	0.907	0.192	-0.023	-0.014	<.01
Spleen	0.867	0.941	0.213	-0.024	0.009	0.27
Gallbladder	0.438	0.491	0.338	-0.089	-0.056	<.01
Pancreas	0.277	0.286	0.197	-0.076	-0.085	<.01
Right Adrenal Gland	0.084	0.027	0.151	-0.119	-0.082	<.01
Left Adrenal Gland	0.190	0.090	0.23	-0.118	-0.141	<.01

Table 4: Comparison of multi-organ segmentation performance without negative prompts. For each organ, the table shows the mean, median, and standard deviation. The mean difference and median difference columns represent the change when negative prompts are excluded (negative values indicate lower performance without prompts). The *P* value shows the results of Wilcoxon signed-rank tests comparing performance with and without negative prompts for each organ.

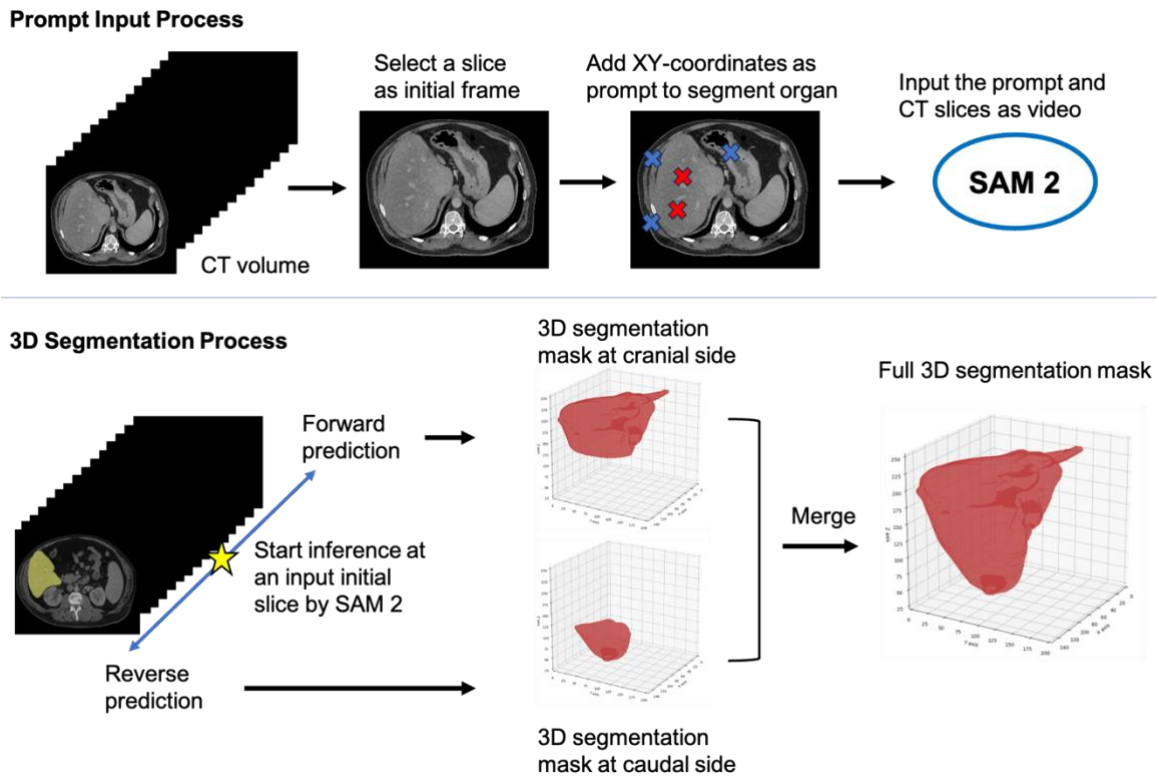


Figure 1: Workflow of 3D Medical Image Segmentation Using SAM 2. This figure illustrates a two-stage process for 3D medical image segmentation. The top row shows the Prompt Input Process, where a slice is selected from a CT volume as an initial frame, and XY-coordinates are added as prompts for organ segmentation (red crosses: positive prompts, blue crosses: negative prompts). These are then input into SAM 2. The bottom row depicts the 3D Segmentation Process, where SAM 2 performs forward and reverse predictions to generate 3D segmentation masks at both cranial and caudal sides. These masks are ultimately merged to create a full 3D segmentation mask of the target organ.

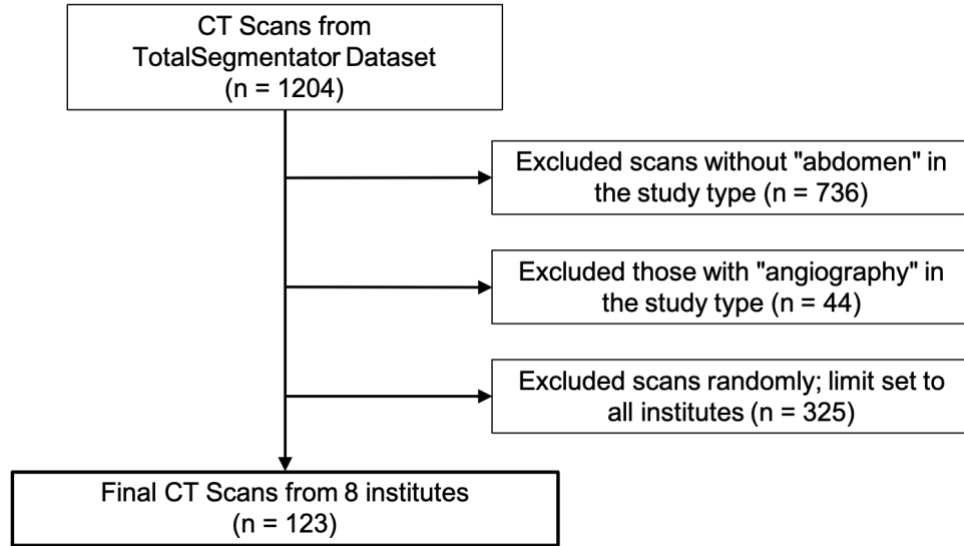


Figure 2: Flow diagram illustrating the CT scan selection process from the TotalSegmentator dataset for evaluation of SAM 2.

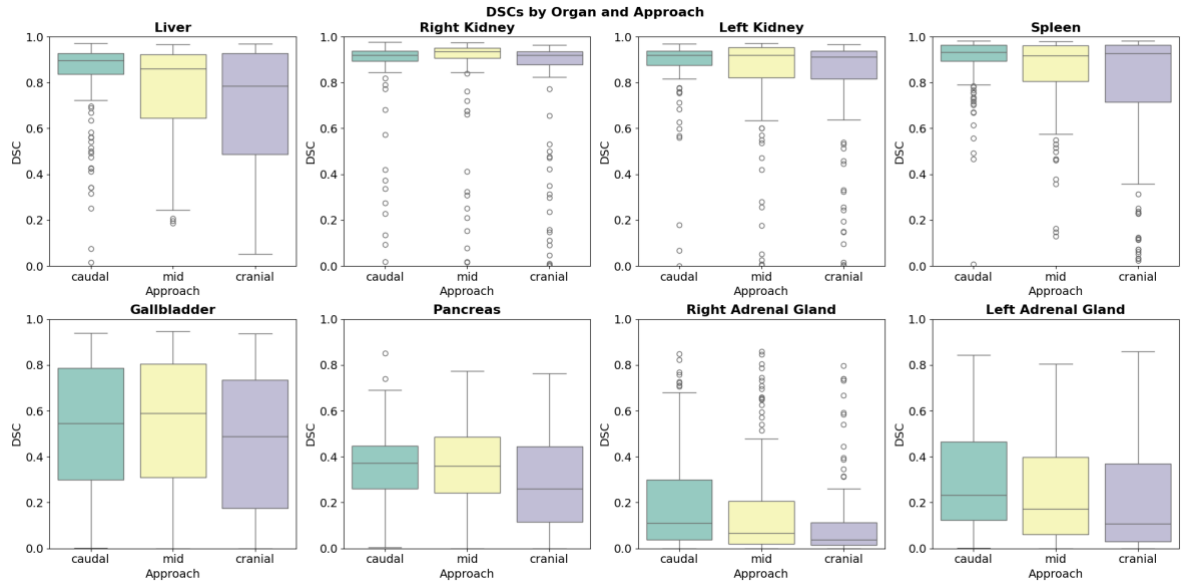


Figure 3: Box plots of DSCs for eight organs (displayed in separate subplots) across three approaches: caudal-approach, mid-approach, and cranial-approach. Each subplot shows the distribution of Dice scores (y-axis, range 0-1) for a specific organ, with the three approaches compared along the x-axis.



Figure 4: Successful segmentation results for eight abdominal organs. Each row shows a different organ with ground truth (left) and predicted (right) 3D masks. Values in parentheses indicate the DSC for each segmentation.

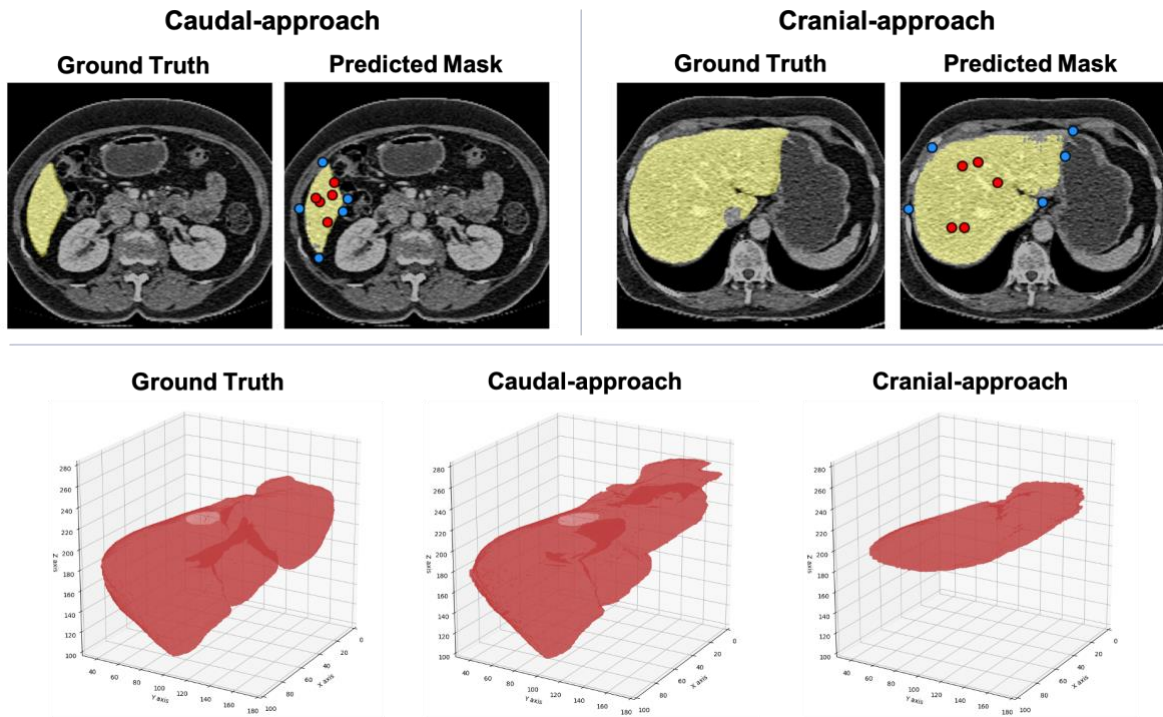
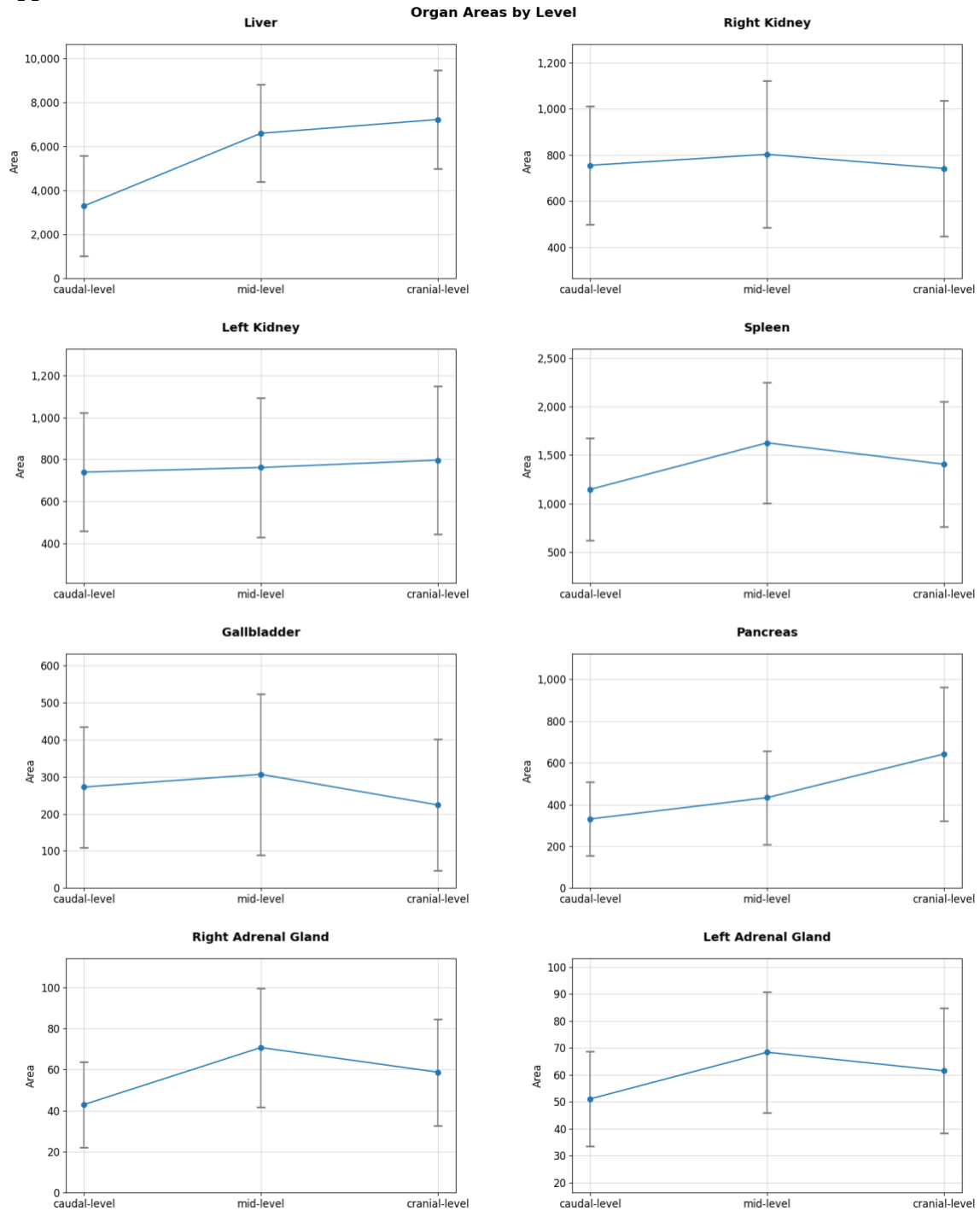
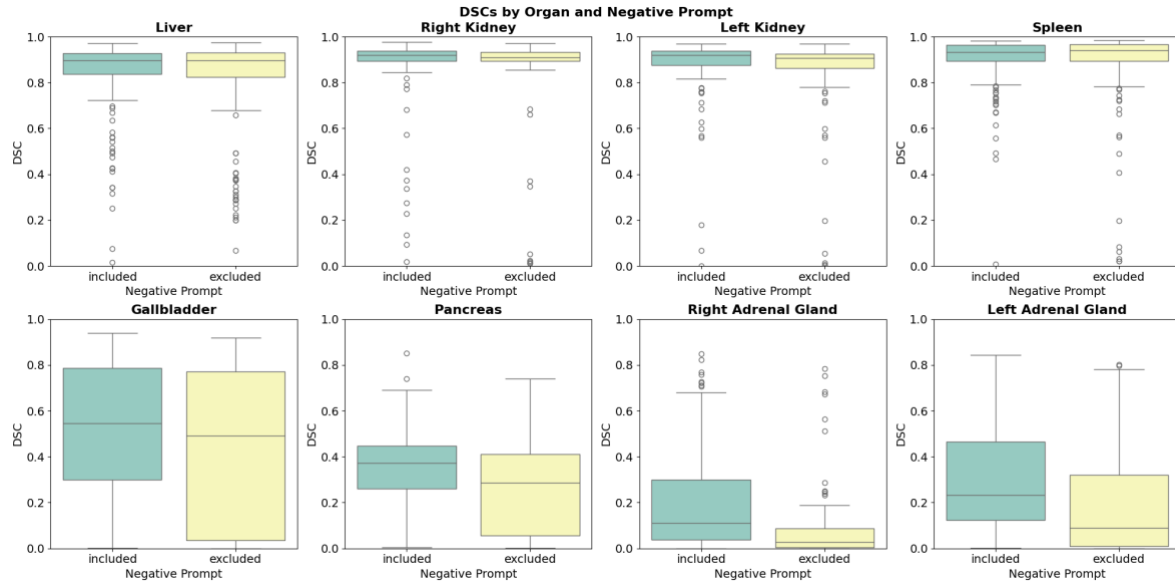


Figure 5: Comparison of segmentation results using caudal-approach and cranial-approach, showing 2D axial slices with Ground Truth and Predicted Mask for both initial slices (top row, with yellow representing the ground truth of liver, blue and red points indicating negative and positive prompts, respectively), alongside 3D renderings of liver segmentation for Ground Truth, Caudal-approach, and Cranial-approach (bottom row).

Supplemental Materials



Supplemental Figure 1: Comparison of organ areas across different levels. The graph displays the mean areas (in voxel) of organs at the caudal-level, mid-level, and cranial-level. Error bars represent standard deviations.



Supplemental Figure 2: Box plots comparing DSCs for eight organs with and without the inclusion of negative prompts. For each organ, DSC values are compared between two conditions: when negative prompts are included (left boxes) and when they are excluded (right boxes).